Received: Added at production | Revised: Added at production | Accepted: Added at production

DOI: xxx/xxxx

ORI

Uncertainty quantification of a thrombosis model considering the clotting assay PFA-100®

Rodrigo Méndez Rojano[1] | Mansur Zhussupbekov[1] | James F. Antaki[1] | Didier Lucor[2]

[1]Meinig School of Biomedical Engineering, Cornell University, NY, USA
[2]Laboratoire Interdisciplinaire des Sciences du Numérique, CNRS, Université Paris-Saclay, Orsay, France

Correspondence
Rodrigo Méndez Rojano, Email: rm2235@cornell.edu

Present Address
Meinig School of Biomedical Engineering
Weill Hall, Room 109

Abstract

Mathematical models of thrombosis are currently used to study clinical scenarios of pathological thrombus formation. As these models become more complex to predict thrombus formation dynamics high computational cost must be alleviated and inherent uncertainties must be assessed. Evaluating model uncertainties allows to increase the confidence in model predictions and identify avenues of improvement for both thrombosis modeling and anti-platelet therapies. In this work, an uncertainty quantification analysis of a multi-constituent thrombosis model is performed considering a common assay for platelet function (PFA-100®). The analysis is facilitated thanks to time-evolving polynomial chaos expansions used as a parametric surrogate for the full thrombosis model considering two quantities of interest; namely, thrombus volume and occlusion percentage. The surrogate is thoroughly validated and provides a straightforward access to a global sensitivity analysis via computation of Sobol' coefficients. Six out of fifteen parameters linked to thrombus consitution, vWF activity, and platelet adhesion dynamics were found to be most influential in the simulation variability considering only individual effects; while parameter interactions are highlighted when considering the total Sobol' indices. The influential parameters are related to thrombus constitution, vWF activity and platelet to platelet adhesion dynamics. The surrogate model allowed to predict realistic PFA-100® closure times of 300,000 virtual cases that followed the trends observed in clinical data. The current methodology could be used including common anti-platelet therapies to identify scenarios that preserve the hematological balance.

KEYWORDS:
Thrombosis, PFA-100®, uncertainty quantification, polynomial chaos expansion, sensitivity analysis

1 | INTRODUCTION

Thrombosis, which is defined as excessive formation of blood clot or thrombus, is a common pathology in several cardiovascular diseases[1], and blood-wetted medical devices[2,3,4]. Thrombus formation is characterized by an intertwined process of platelet activity and coagulation. In this hemostatic process, platelet activation and aggregation leads to formation of a platelet plug that is mechanically stabilized by a fibrin net formed by coagulation reactions[5]. In hemodynamic conditions that promote high shear stresses, such as stenotic vessels or prosthetic heart valves or blood pumps, von Willebrand Factor (vWF) plays a central role in thrombosis. vWF is a blood glycoprotein that has a collapsed globular conformation in its natural state and unfolds in response

to extensional flow and high-shear flow conditions. Once unfolded, vWF plays an important role in the platelet adhesion and aggregation process enabling clot formation.

Multi-scale computational models of thrombosis have been developed in the past decades to understand and predict the thrombus formation dynamics in academic and clinical configurations ([6,7,8,9,10,11,12]). These models span several degrees of complexity, from simple flow characteristic indices to complicated, coupled biochemical interactions. Mechanistic models, for example, may contain equations that describe shear dependent platelet activity including adhesion, aggregation, and activation[13,14,15]; hemodynamics that regulate the transport of biochemical species[16,17]; and/or coagulation reactions that lead to the formation of fibrin[18,19,20]. Increasing modeling complexity improves the fidelity and versatility of the model, but the computational cost of the simulation escalates. Also, increasing detail introduces additional uncertainties that can have a great impact on its accuracy[21]. These uncertainties are related to the fundamental structure of the model , numerical discretization, and/or model parameters such as diffusion coefficients, concentrations of biochemical species, fluid viscosity, etc. Previous investigators have introduced several uncertainty quantification (UQ) strategies to evaluate the effect of such uncertainties on model performance in the context of blood flows[22,23,24,25]. UQ analyses in thrombosis models have been performed to identify the sensitivity of input parameters[26,27,28,29]. In most sensitivity studies, the global Morris method[30] or the Sobol' indices method[31] have been used. The Morris method is used as a screening tool to identify important parameters in models with a large number of input variables. The Sobol' method produces indices based on variance that quantifies the output uncertainty related to each input parameter. For example, Melito et al.[29] performed a variance based sensitivity analysis on the thrombosis model of Menichini et al.[7] considering thrombosis in a backward facing step. Their results suggest that only four of the nine parameters included in their thrombosis model had significant impact in thrombus formation implying that the model could be made sparser to optimize computational resources. Link et al.[32] performed a sensitivity analysis to identify important coagulation factors in the thrombin generation profile among hemophilia A patients. Their work allowed the identification of coagulation factor V as an important modifier of thrombin formation among patients with hemophilia A, paving the way to pharmacological interventions to treat these patients. In addition, as demonstrated by Link et al.[32] the synthetic databases built to perform sensitivity analysis can serve as hypothesis generation tool for *in-vitro* experiments or, in the long run, patient treatment.

In this work, a forward uncertainty propagation study is conducted using a well-established but computationally costly multi-constituent thrombosis model introduced by Wu et al.[33]. A widely used platelet function assay PFA-100® (Siemens, Erlangen, Germany) was selected as the study case. To understand the impact of uncertain input parameters a variance based global sensitivity analysis was conducted monitoring Sobol' sensitivity coefficients taking advantage of a polynomial chaos approximation as a surrogate of the baseline thrombosis model. The surrogate model is also used in this study to assess its predictive ability of the PFA-100® closure time distribution in three scenarios: normal platelet count, thrombocytopenia, and vWF deficiency. The predicted closure times distribution align well with clinical data.

2 | METHODS

2.1 | Baseline Thrombosis Model

The thrombosis model used in the current work is a variation of the approach introduced by Wu et al.[33] with the addition of vWF activity. Figure 1 A shows how platelets, the central player of the model, deposit to artificial surfaces. Figure 1 B illustrates vWF unfolding due to high shear rates increasing platelet deposition. Thrombus growth is quantified through platelet deposition over artificial surfaces and subsequent platelet aggregation. Several biochemical species are considered in the model: 1) **AP** Activated platelets, 2) **RP** Resting Platelets, 3) $\mathbf{AP}_d$ Deposited activated platelets, 4) $\mathbf{RP}_d$ Deposited Resting Platelets 5) **ADP** Adenosine Diphosphate, 6) $\mathbf{TxA}_2$ Thromboxane A2, 7)**TB** Thrombin , 8) **PT** Prothrombin, 9) **AT** Anti-Thrombin, 10) $\mathbf{vWF_c}$ vWF Coiled, and 11) $\mathbf{vWF_s}$ vWF stretched.

The spatial and temporal dynamics of biochemical species are quantified through convection-diffusion-reaction equations of the form:

$$\frac{\partial c_i}{\partial t} = \nabla \cdot (D_i \nabla c_i) - \boldsymbol{v}_f \cdot \nabla c_i + r_i, \tag{1}$$

where: c_i is the concentration of species i, D_i is the diffusion coefficient, $\boldsymbol{v}_f$ is the velocity vector field, and r_i is the reaction source term that accounts for biochemical interactions such as platelet activation by thrombin or TxA_2.

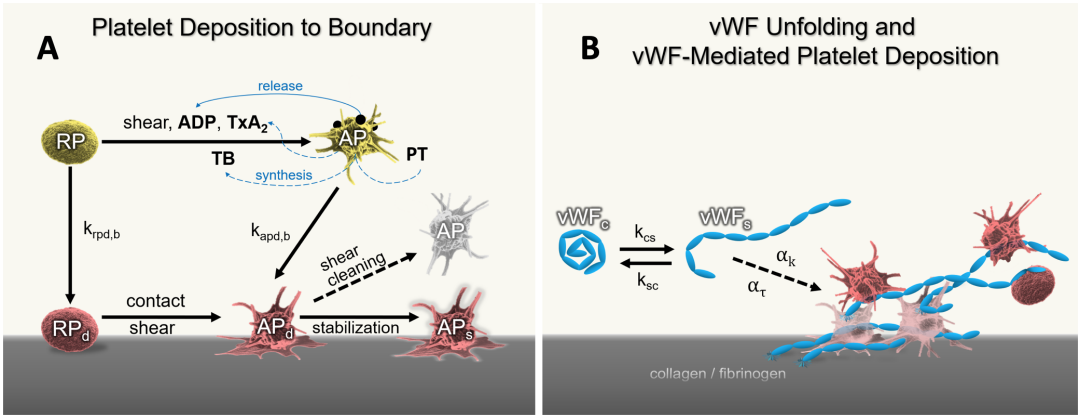

FIGURE 1 A) Diagram of platelet activation and deposition in the thrombosis model. $k_{rpd,b}$ and $k_{apd,b}$ are the rates at which resting and activated platelets deposit to the surface. Resting platelets can be activated by mechanical shear, or the combination of agonists: ADP, TxA_2 and thrombin. Once deposited, AP_d can stabilize or embolize due to flow shearing forces. B) Schematic depiction of vWF unfolding and vWF-mediated platelet deposition and aggregation. The presence of stretched vWF_s amplifies the deposition rate of free-flowing platelets by α_k and increases the resistance of deposited platelets to shear cleaning by α_τ.

2.1.1 | vWF activity

To account for the role of vWF in high shear stress thrombosis the original model of Wu et al.[33] was amended to include the enhanced platelet aggregation and adhesion driven by vWF activity. The right-hand side of Figure 1 shows the two interconvertible states of vWF in the model: collapsed vWF_c and stretched vWF_s . In all simulations, only vWF_c is introduced at the inlet of the domain and vWF_s is produced by means of vWF_c unfolding. The presence of stretched vWF_s polymers has a local thrombogenic effect via two mechanisms: it amplifies the deposition rate of free-flowing platelets by scaling it by α_k (Eq (2)) and increases the resistance of deposited platelets to shear cleaning by scaling the shear-cleaning parameters, τ_{emb} and $\tau_{emb,b}$, by α_τ according to Eq (3)

$$\alpha_k = \begin{cases} 1, & \text{if } \mathrm{vWF_s} \le \mathrm{vWF_s^{crit}} \\ \frac{\mathrm{vWF_s}}{\mathrm{vWF_s^{crit}}}, & \text{if } \mathrm{vWF_s} > \mathrm{vWF_s^{crit}} \end{cases} \tag{2}$$

$$\alpha_\tau = \begin{cases} 1, & \text{if } \mathrm{vWF_s} \le \mathrm{vWF_s^{crit}} \\ \frac{D_e(\dot\gamma)}{D_e^l}, & \text{if } \mathrm{vWF_s} > \mathrm{vWF_s^{crit}} \end{cases}, \tag{3}$$

where $\mathrm{vWF_s^{crit}}$ is set as 5% of the total vWF concentration; D_e is the Morse potential's well depth proposed by Yazdani et al.[8] that correlates the platelet adhesion force to the local shear rate, $\dot\gamma$, according to Eq (4);

$$D_e(\dot\gamma) = D_e^h \left[\tanh\left(\frac{\dot\gamma - \dot\gamma_{vWF}}{1000} \right) + \frac{D_e^l}{D_e^h} + 1 \right], \tag{4}$$

D_e^l and D_e^h determine the adhesive forces at low and high shear rates, respectively, and $\dot\gamma_{vWF} = 5500\ \mathrm{s^{-1}}$ is the critical shear rate for vWF unfolding and marks the transition from low-shear to high-shear regime in this expression. The value for D_e^l, D_e^h, $\mathrm{vWF_s^{crit}}$, and $\dot\gamma_{vWF}$, were obtained from Yazdani et al.[8]. The scalar shear rate $\dot\gamma$ is computed following OpenFoam source code[34]:

$$\dot\gamma = \sqrt{2Tr(symm(\nabla \boldsymbol{u}) \cdot symm(\nabla \boldsymbol{u}))} \tag{5}$$

vWF_c unfolding occurs via two mechanisms: periodic tumbling in simple shear and strong unfolding in flows with extensional kinematics. The flow classification is based on polymer unfolding criteria by Babcock et al.[35] where they define the flow-type λ as:

$$\lambda = \frac{\|\boldsymbol{S}\| - \|\boldsymbol{\Omega}\|}{\|\boldsymbol{S}\| + \|\boldsymbol{\Omega}\|} \tag{6}$$

where $\|\boldsymbol{S}\|$ and $\|\boldsymbol{\Omega}\|$ are the magnitudes of the symmetric and anti-symmetric parts of the velocity gradient tensor, respectively. Thus, in the limiting cases of the flow type parameter, $\lambda = 1$ corresponds to purely extensional flow, $\lambda = 0$ to simple shear

flow, and $\lambda = -1$ to solid-body rotation. vWF will experience strong unfolding in flows with $\lambda \geq \lambda_{crit}$, simple-shear tumbling in $-\lambda_{crit} \leq \lambda < \lambda_{crit}$, and remain collapsed if $\lambda < -\lambda_{crit}$.

In simple shear and near-shear flows, $-\lambda_{crit} \leq \lambda < \lambda_{crit}$, the unfolding rate, $k_{c\text{-}s}$ (collapsed-to-stretched conversion), follows a function proposed by Lippok et al.[36] for shear-dependent cleavage rate of vWF. Since this function describes the availability of vWF monomers for enzymatic cleavage, the unfolding rate is assumed to follow the same shape, given by Eq. (7)

$$k_{c\text{-}s}^{shear}(\dot{\gamma}) = \frac{k'}{1 + \exp\left(-\frac{\dot{\gamma} - \dot{\gamma}_{vWF}}{\Delta\dot{\gamma}}\right)} \tag{7}$$

$$k_{s\text{-}c}^{shear} = k' \tag{8}$$

where $\dot{\gamma}_{vWF} = 5500$ s^{-1} is the critical (half-maximum) shear rate for vWF unfolding and $\Delta\dot{\gamma} = 1271$ s^{-1} denotes the width of the transition. k' is the nominal state conversion rate, given by $k' = 1/t_{vWF}$, where $t_{vWF} = 50$ ms is the vWF unfolding time. This timescale for vWF unfolding was reported in experiments by Fu et al.[37] and Brownian dynamics simulations by Dong et al.[38,39] To reflect the tumbling behavior of the vWF in this regime, the stretched-to-collapsed conversion rate, $k_{s\text{-}c}$ is set to the nominal value k' (Eq. (8)).

In extensionally-dominated flows with $\lambda \geq \lambda_{crit}$, strong unfolding occurs if the modified Weissenberg number, Wi_{eff}, given by Eq. (9), exceeds the critical value $Wi_{eff,crit}$. Then, the unfolding rate $k_{c\text{-}s}^{steady}$ scales with Wi_{eff} according to Eq. (10), while $k_{s\text{-}c}^{steady}$ is zero.

If Wi_{eff} falls below $Wi_{eff,crit}$, the stretched vWF$_s$ exhibits hysteresis and does not collapse back to vWF$_c$ until $Wi_{eff} < Wi_{eff,hyst}$, as shown in Eq. (11).

$$Wi_{eff} = \sqrt{\lambda}\,(\|\boldsymbol{S}\| + \|\boldsymbol{\Omega}\|)\,\tau_{rel} \tag{9}$$

$$k_{c\text{-}s}^{steady} = \begin{cases} k' \frac{Wi_{eff}}{Wi_{eff,crit}}, & \text{if } Wi_{eff} \geq Wi_{eff,crit} \\ k_{c\text{-}s}^{shear}, & \text{if } Wi_{eff} < Wi_{eff,crit} \end{cases} \tag{10}$$

$$k_{s\text{-}c}^{steady} = \begin{cases} 0, & \text{if } Wi_{eff,hyst} \leq Wi_{eff} < Wi_{eff,crit}. \\ k', & \text{if } Wi_{eff} < Wi_{eff,hyst}. \end{cases} \tag{11}$$

where τ_{rel} is the polymer relaxation time used to non-dimensionalize the expression. Here, we adopted the unfolding threshold and the hysteresis value reported by Sing and Alexander-Katz.[40] Assuming the monomer diffusion time of 1.02×10^{-3} s for τ_{rel} in Eq. (9), $Wi_{eff,crit} = 0.316$ and $Wi_{eff,hyst} = 0.053$.

If $\lambda < -\lambda_{crit}$, vWF$_c$ remains collapsed and vWF$_s$ reverts to a globular state, so $k_{c\text{-}s} = 0$ and $k_{s\text{-}c} = k'$.

The reaction term for vWF$_c$ and vWF$_s$ is then obtained by multiplying the reaction rates previously described by the concentration of this species following the law of mass action. A detailed validation of the vWF-thrombosis model is provided in Zhussupbekov et al.[41] for multiple academic simple flow configurations and complex in-vitro clotting scenarios.

2.1.2 | Flow dynamics

The pressure and velocity fields p and $\boldsymbol{v}_f$ are obtained solving the Navier-Stokes equations considering an incompressible Newtonian fluid:

$$\frac{\partial \rho_f}{\partial t} + \nabla \cdot (\rho_f \mathbf{v}_f) = 0 \tag{12}$$

$$\rho_f \frac{D\mathbf{v}_f}{Dt} = \nabla \cdot \mathbf{T}_f + \rho_f \mathbf{b}_f + C_2 f(\phi)(\mathbf{v}_f - \mathbf{v}_T) \tag{13}$$

where $\mathbf{T}_f$ is the stress tensor of the fluid described as:

$$\mathbf{T}_f = [-p(1-\phi)]\mathbf{I} + 2\mu_f(1-\phi)\mathbf{D}_f \tag{14}$$

where μ_f is the asymptotic dynamic viscosity of blood. The scalar field ϕ is introduced to represent the volume fraction of deposited platelets (thrombus). $\mathbf{D}_f$is the symmetric part of velocity gradient. The fluid phase density ρ_f is defined as

$$\rho_f = (1-\phi)\rho_{f0} \tag{15}$$

where ρ_{f0} is the density reference value of the fluid phase, $\mathbf{b}_f$ is the body force, $\mathbf{v}_f$ is and $\mathbf{v}_T$ are the velocity of the fluid and thrombus phases, respectively. C_2 is the resistance constant assuming that deposited platelets are densely compact spherical particles (2.78 μm), $f(\phi) = \phi(1 + 6.5\phi)$ is the hindrance function. For a full description of the original thrombosis model the reader is referred to the work of Wu et al.[33] and Sorensen et al.[13].

2.2 | Case of Study PFA-100®

The platelet function analyzer PFA-100® (Siemens Erlangen, Germany) is a coagulation testing device that is used to assess the primary hemostasis response[42]. Figure 2 shows a cross section sketch of the PFA-100® test cartridge whose main component is a bio-active membrane with a central orifice of 140 microns diameter. Whole blood is aspirated through a capillary towards the membrane, as blood flows through the central orifice of the membrane, a thrombus forms until occlusion is achieved. The membrane is coated with collagen and epinephrine or ADP to promote thrombus formation. Flow is driven by a vacuum system that applies a Δp of 4000 Pa. Shear rates inside the orifice reach values up to 6000 s^{-1} promoting vWF unfolding leading to preferential thrombus formation[43] inside the membrane orifice. When the orifice is fully occluded a Closure Time (CT) is obtained which is the quantity used to diagnose patients. The normal CTs are in the range 79-139 s for epinephrine cartridges and 61-105 s for ADP cartridges[42]. Prolonged CT times are observed in patients with major platelet defects (Bernard Soulier syndrome, Glanzmann's thrombasthenia, thrombocytopenia, etc.) and vWF disease, or acquired vWF disease, among others[42]). In addition, CT times are affected by a variety of hematological and pharmacological factors such as hematocrit and aspirin.

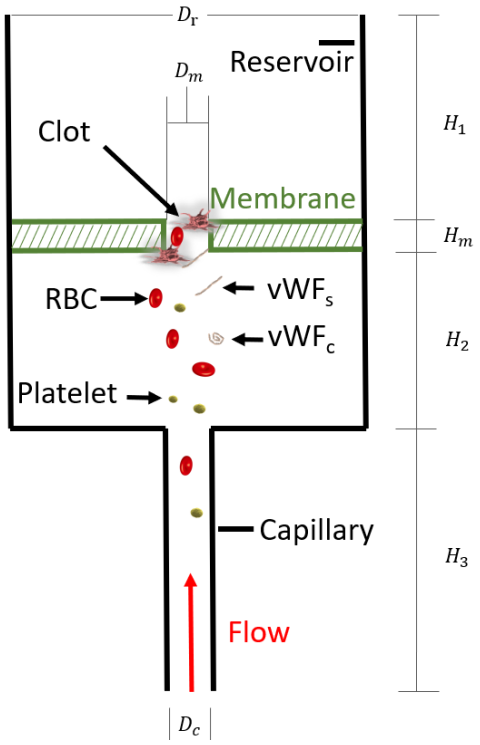

FIGURE 2 Cross section of PFA-100® testing cartridge showing the capillary, the central membrane with orifice, and reservoir. As whole blood is aspired through the cartridge blood constituents aggregate in the coated membrane orifice. The dimensions of the PFA-100 cartridge as considered in the simulations are: $D_c = 200$, $D_m = 147$,$D_r = 1200$, $H_1 = 1000$, $H_2 = 400$, $H_3 = 1200$, and $H_m = 200$ all in μm.

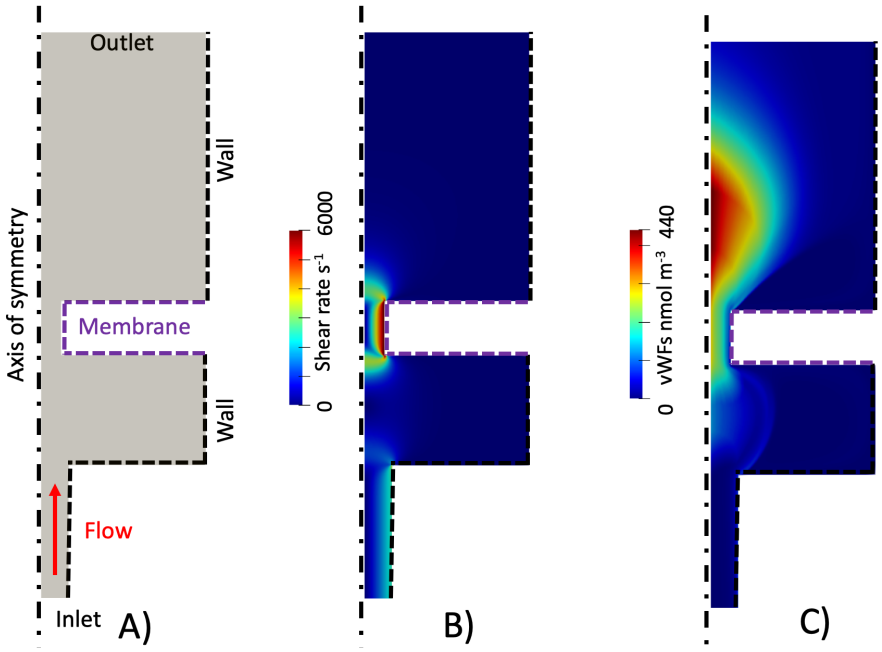

FIGURE 3 A) Numerical setup of PFA-100® thrombosis simulation. The membrane is set as reactive boundary condition allowing platelet deposition. B) Scalar shear rate field, large shear rates are observed in the membrane orifice. C) concentration of stretched vWF (vWFs) illustrating unfolding within and downstream of the membrane orifice.

2.3 | Baseline Thrombosis Simulation

An axisymmetric thrombosis simulation of the PFA-100® assay is the baseline case for the uncertainty quantification analysis. Figure 3A shows the setup of the simulation. A uniform velocity profile $\mathbf{v}_f = (0, 0.127, 0)$ m s^{-1} was set at the inlet boundary. This boundary condition was used to avoid numerical instabilities observed in pressure driven flows. The membrane and cartridge walls were set as no-slip boundary conditions. A zero gradient velocity boundary condition was considered at the outlet. The pressure the outlet boundary was set to zero, and a zero gradient boundary condition was set for all remaining boundaries. In terms of biochemical species Table 1 lists the blood constituents concentrations that were prescribed at the inlet boundary. The platelet count values are representative of patients treated with ventricular assist devices[44]. At the outlet and cartridge walls a zero gradient boundary condition was applied for the species concentration. To reflect the ADP-collagen coated membrane, a reactive boundary condition was prescribed over the membrane to specify the region in which platelets are allowed to deposit. In addition, a diffusive flux of ADP $= 1 \times 10^7$ nmol m^{-2} s^{-1} was prescribed to mimic shedding of ADP coating from the membrane. The ADP flux value was determined by best fit to clinical occlusion times reported by Steinlechner et al.[44]. All remaining variables were derived from the literature. The diffusion coefficient for each biochemical species were taken from[45]. We employed a Newtonian constitutive model for blood with a viscosity of 3.5 cP and a density of 1050 kg m^{-3}. The parameter values describe along Section 2.1.1 were used in the baseline thrombosis simulation.

The computational mesh was composed of 68650 hexahedral cells with a finest resolution of $\Delta x = 3$ μm located in the membrane orifice. A dual time step strategy was used to economize computational cost. A time step of $\Delta t_{CDR} = 1 \times 10^{-3}$ s was used to solve the species equations and thrombus growth. The flow equations are solved with a time step $\Delta t_{CFD} = \Delta t_{CDR}/r_{flow} = 1 \times 10^{-8}$ s, ensuring the Courant–Friedrichs–Levy stability condition CFL ≤ 1, this strategy has been previously used in multi-scale platelet activation simulations[46]. A parametric study with different values of the scaling factor r_{flow} spanning four orders of magnitude was performed to show the robustness of the approach (See Supporting Information). Before running the thrombosis simulation, a steady state flow solution was obtained to improve stability at the first instants of the thrombosis simulation. The resulting shear rate field was computed corroborating that inside of the membrane orifice induced shear rates greater than 6000 s^{-1} required for vWF stretching. (See Figure 3B and C.)

Figure 4A shows the thrombus formation at 100 seconds of simulation, the blood clot is visualized through a platelet volume fraction threshold > 0.8. Thrombus is formed inside the membrane orifice within the time scales observed clinically in VAD

Species	Concentration
RP	216 $\times 10^3$ Plt μL^{-1}
AP	2.16 $\times 10^3$ Plt μL^{-1}
vWF_c	1000 nmol m^{-3}
PT	1.1$\times 10^6$ nmol m^{-3}
TB	0 nmol m^{-3}
AT	2.844 $\times 10^6$ nmol m^{-3}
ADP	0 nmol m^{-3}
TxA_2	0 nmol m^{-3}

TABLE 1 Blood constituents inlet concentrations, the platelet count is representative of patients treated with ventricular assist devices[44].

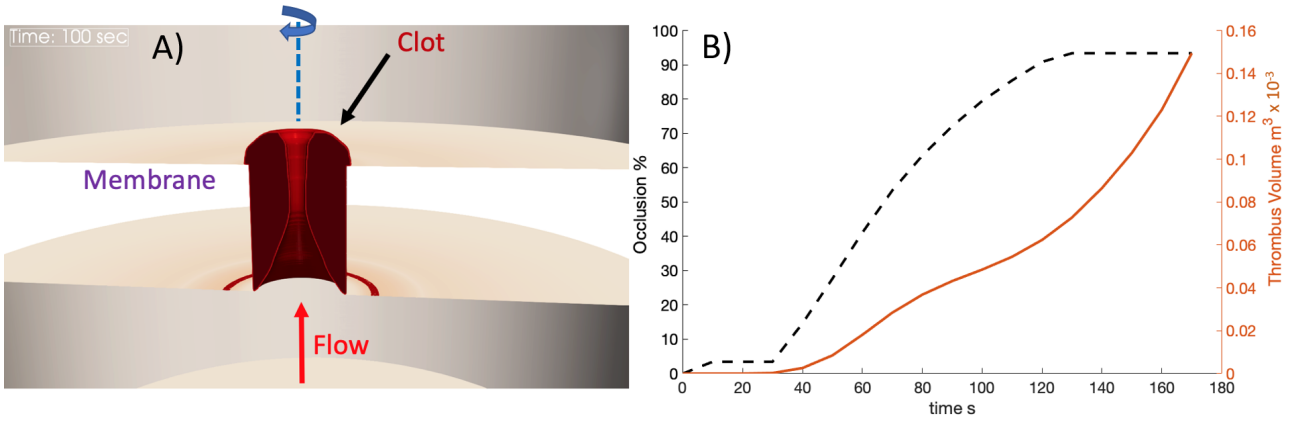

FIGURE 4 A) 3D rotational extrusion view of thrombus formation at 100 seconds of simulation, clot forms inside the membrane orifice. The blue line and arrow denote the rotation axis to obtain the 3D view. B) Quantities of interest $(Y(X_i))$ for the UQ analysis, occlusion percentage across the top edge of the membrane (dashed line) and total thrombus volume inside (solid line).

patients (80-150 s)[44], the simulation closure time is defined at 80 % of occlusion since full thrombotic closure is not numerically achievable due to exponential increase of mechanical shear prompting thrombus cleaning and preventing full occlusion. The main mechanism that drives clot formation can be explained as follows: 1) platelets deposit on the collagen coated membrane, 2) ADP within the membrane amplifies platelet activity, 3) large shear rates inside the membrane promote both platelet activation and vWF unfolding, further amplifying platelet deposition, 4) as the clot grows, the orifice area is reduced further increasing shear rates, which increases vWF activity forming a positive feedback loop mechanism. The quantities of interest (QoIs) chosen for the UQ analysis, described below, are: (1) the percentage of occlusion over the top edge plane of the membrane and (2) the total thrombus volume in the domain. These quantities are plotted in Figure 4B.

In order to show the importance of including the vWF unfolding dynamics and its influence on the platelet adhesion process, a simulation imposing vWF_c inlet condition to zero was performed. This simulation corresponds to the original model of Wu et al. Figure 5 A shows the absence of clot without vWF_c . The platelet deposition rates for both cases are presented in Fig. 5 B showcasing that vWF activity increases the deposition rates inside the membrane promoting thrombus formation.

2.4 | Uncertainty Quantification

2.4.1 | Identification and modeling of random sources

The thrombosis model used in this study is one of the most realistic models up to-date for medical devices[47]. In the following we will therefore put aside the model uncertainty in terms of its structure, complexity and underlying numerical algorithmic and we will focus only on physical parametric uncertainty. The model involves a total of 68 parameters (diffusion coefficients, reaction rates, biochemical concentrations, viscosity, density, etc). The uncertainties related to the microfluidic assay geometry

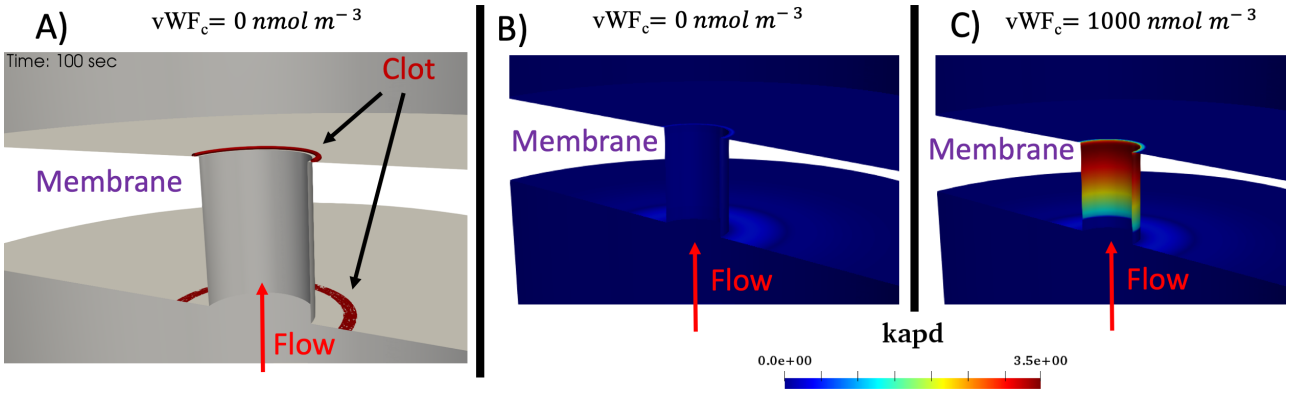

FIGURE 5 Thrombosis simulation with inlet condition $\text{vWF}_c = 0$ nmol m^{-3} which corresponds to the original model of Wu et al.[33]. A) Lack of thrombus formation at 100 seconds with inlet boundary condition $\text{vWF}_c = 0$ nmol m^{-3}. B) Platelet deposition rate k_{apd} for $\text{vWF}_c = 0$ nmol m^{-3}, and C) Platelet deposition rate k_{apd} for $\text{vWF}_c = 1000$ nmol m^{-3}.

were not considered as they are not as important as in physiological vessel hemodynamics. Due to the computational cost of performing an analysis considering all the model parameters (64 core-hours per simulation), we have selected a subset of 15 influential parameters based on our experience gained from previous thrombosis simulations in both macroscopic and microscopic configurations[48,33,49,41]. The parameters are listed in Table 2 with their definition and distribution values. The literature does not show evidence of particular type of uncertainty distributions for these parameters. At best only low-order statistics are available (i.e. mean and standard deviation), which implies (under a maximum entropy principle) to model the distributions as normally distributed. For sake of simplicity, independent Gaussian probability distributions were assumed for the parameters. Moreover, in order to introduce a similar level of uncertainty for all input parameters, we set the standard deviation to be ten percent of the mean value for each parameter, cf. Table 2. This choice was done to avoid bias in the selection of the standard deviation value for each parameter as they are not well characterized in the literature.

Parameter X_i	Definition	Distribution (mean, standard deviation)
1) RP	Resting platelets	$\mathcal{N}(216\times10^3, 21.6\times10^3)$ Plt μL^{-1}
2) AP	Activated platelets	$\mathcal{N}(2160, 216)$ Plt μL^{-1}
3) vWF_c	vWF concentration	$\mathcal{N}(1000, 100)$ nmol m^{-3}
4) K_{rpd}	Deposition rate RP (to membrane)	$\mathcal{N}(1.0\times10^{-8}, 1.0\times10^{-9})$ m s^{-1}
5) K_{apd}	Deposition rate AP (to membrane)	$\mathcal{N}(3.0\times10^{-6}, 3.0\times10^{-7})$ m s^{-1}
6) K_{aa}	Deposition rate of AP to AP_d	$\mathcal{N}(3.0\times10^{-5}, 3.0\times10^{-6})$ m s^{-1}
7) K_{ra}	Deposition rate of RP to AP_d	$\mathcal{N}(3.0\times10^{-6}, 3.0\times10^{-7})$ m s^{-1}
8) $\dot{\gamma}_{vWF}$	critical shear rate for vWF unfolding	$\mathcal{N}(5500, 550)$ s$^-1$
9) $\Delta\dot{\gamma}$	vWF shear unfolding transition width	$\mathcal{N}(1271, 127.1)$ s^2
10) λ_{crit}	Flow type critical value for strong unfolding	$\mathcal{N}(0.005, 0.0005)$ dimensionless
11) t_{vWF}	vWF relaxation time	$\mathcal{N}(0.05, 0.005)$ s
12) $Wi_{eff,crit}$	Wi_{eff} critical value for strong unfolding	$\mathcal{N}(0.316, 0.0316)$ dimensionless
13) $Wi_{eff,hyst}$	Wi_{eff} hysteresis value	$\mathcal{N}(0.053, 0.0053)$ dimensionless
14) $\text{vWF}_s^{\text{crit}}$	Critical vWF_s concentration value	$\mathcal{N}(50, 5)$ nmol m^{-3}
15) D_e^h / D_e^l	Ratio of adhesive forces at high and low shear rates	$\mathcal{N}(500, 50)$ dimensionless

TABLE 2 Fifteen (15) parameters of the thrombosis model.

2.4.2 | Polynomial chaos surrogate modeling framework

Numerical simulation of blood flow problems are nowadays more common, mainly because of increasing computational power, progress in imaging and numerical algorithms. Nevertheless, it remains very costly to quantify the link between multi-physics, multi-scale and multi-parameters phenomena to useful clinical indicators. A large number of model order reduction techniques have been proposed, e.g.[50,51].

In order to alleviate the computational cost of a parametric study involving the full thrombosis model, a surrogate model will be constructed in place of the direct thrombosis model. The surrogate model should approximate the quantity of interest Y as accurately as possible. We remind the reader that this is not an obvious task in case one is interested in multiple quantities of interest. A continuous surrogate is constructed from a finite set of the thrombosis model predictions for some selected parameter values in a "off-line" stage, and subsequently used "in-line" during the prediction stage. To this end, different methods are available such as Gaussian processes[52], support vector machines[53], stochastic interpolation[54], or stochastic spectral methods such as polynomial-based representations. Polynomial chaos expansions (PCE) will be retained to express the surrogate model in a closed form[55,56] and some formulations exist to *adaptively* construct the approximation functionals satisfying some optimality criteria, e.g.[57]. Let $(\Omega, \mathcal{B}, \mathcal{P})$ be the probability space where Ω is the space of random events ω, this domain has a σ-algebra $\mathcal{B}$ and is equipped with a probability measure $\mathcal{P}$. The vector of normally-distributed random parameters can be written as $\boldsymbol{X} \equiv \boldsymbol{X}(\omega) = (X_1, \dots, X_{d=15})$. If we consider, at a given time instant, the $d-$variate and second-order random variable $Y : \mathcal{I}_{\boldsymbol{X}} \subseteq \mathbb{R}^d \to \mathbb{R}$, then $Y(t, \boldsymbol{X}) \in \ell_2(\Omega, \mathcal{B}, \mathcal{P})$, can be expressed as the following expansion[56]:

$$Y(t, \boldsymbol{X}) = \sum_{j=0}^{\infty} y_j(t)\, \psi_j(\boldsymbol{X}), \tag{16}$$

where $\psi_j(\boldsymbol{X}) = \prod_{i=1}^{d} \psi_j^{(i)}(X_i)$ are the multivariate basis functions that form a complete basis, orthonormal with respect to the probability measure $\rho_{\boldsymbol{X}}$ of the random input, and $\psi_j^{(i)}$ are the univariate Hermite polynomial functions along the i^{th} dimension. In practice, PCE expansion must be truncated, and writes:[1]

$$Y(t, \boldsymbol{X}) \approx \sum_{\boldsymbol{\gamma} \in \beta_p} y_{\boldsymbol{\gamma}}(t)\, \psi_{\boldsymbol{\gamma}}(\boldsymbol{X}), \tag{17}$$

where $y_{\boldsymbol{\gamma}}(t)$ are the evolving *modal* coefficients corresponding to the $\psi_{\boldsymbol{\gamma}}$ basis. For instance, a choice of $p = 2$ corresponds to at most quadratic Hermite polynomials in the variables $\boldsymbol{X}$. We will restrict ourselves to tensor-product polynomial spaces $\mathbb{P}_{\beta_p}$, where β_p is an index set of "degree" p, and where $P = \dim(\mathbb{P}_{\beta_p}) \equiv \#\beta_p$, will denote the cardinality of the selected polynomial space. There are different ways of constructing the approximating polynomial spaces that will impact their cardinality. More specifically, in this study we will rely on $q-$norm type of polynomial spaces, allowing for an hyperbolic truncation of the approximation basis (therefore reducing the computational cost): $\mathbb{P}_{\beta_{p,q}}$ with index set $\beta_{p,q} = \{\boldsymbol{y} \in \mathbb{P}_{\beta_p} : \|\boldsymbol{y}\|_q = \left(\sum_{\boldsymbol{\gamma}} y_{\boldsymbol{\gamma}}^q\right)^{1/q} \leq p\}$[58]. By default, the hyperbolic truncation with $q = 1$ reduces to the standard total-degree truncation scheme. Decreasing the value of q *de facto* decreases the number of polynomials of high interaction order kept in the expansion.

2.4.3 | Adaptively constructing the surrogate by least-squares minimization with regularization

Based on a training set $\{\boldsymbol{X}^{(i)}, Y^{(i)}\}_{i=1,\dots,N}$ collected at each time instant, ordinary linear regression can be used to compute the unknown coefficients $\boldsymbol{y} \equiv y_{\boldsymbol{\gamma}}$,[59,60] by minimizing the residuals $\boldsymbol{r} \equiv \boldsymbol{Y} - \boldsymbol{\psi}_{\beta_p} \boldsymbol{y}$ in the ℓ_2-norm through an optimization problem:

$$\boldsymbol{y} = \underset{\mathbf{y} \in \mathbb{R}^P}{\operatorname{argmin}} \|\boldsymbol{Y} - \boldsymbol{\psi}_{\beta_p} \mathbf{y}\|_2^2, \tag{18}$$

where $\boldsymbol{\psi}_{\beta_p}$ is the measurement matrix corresponding to the gPC expansion in the index set β_p. The solution is obtained in matrix form as:

$$\boldsymbol{y} = \left(\boldsymbol{\Psi}_{\beta_p}^{\mathsf{T}} \boldsymbol{\Psi}_{\beta_p}\right)^{-1} \boldsymbol{\Psi}_{\beta_p}^{\mathsf{T}} \mathbf{Y}, \tag{19}$$

where $\mathbf{Y}$ is a vector of observations of size $N \times 1$, $\boldsymbol{\Psi}_{\beta_p}$ the *measurement matrix* of size $N \times P$ with $\Psi_{ij} = \psi_j(\boldsymbol{X}_i)$, and $\boldsymbol{y}$ the vector of coefficients of size $P \times 1$. Unfortunately, when the number of simulations $N < P$, the problem is not well posed under

[1] Instead of indexing the expansion on a single integer amounting to the cardinality of the entire approximation space, one can also make use of a multi-index notation that is equivalent. If β_p is an index set for multi-index $\boldsymbol{\gamma} = (\gamma_1, \dots, \gamma_d) \in \mathbb{N}_0^d$, then $\mathbb{P}_{\beta_p} \equiv \operatorname{span}\{\psi_{\boldsymbol{\gamma}} \mid \boldsymbol{\gamma} \in \beta_p\}$.

this formulation and one needs to add a regularization term in the form of:

$$\boldsymbol{y} = \underset{\mathbf{y}\in\mathbb{R}^P}{\operatorname{argmin}} \frac{1}{2}\|\boldsymbol{Y} - \boldsymbol{\Psi}_{\beta_p}\mathbf{y}\|_2^2 + \beta\|\mathbf{y}\|_1, \tag{20}$$

with $\|\boldsymbol{y}\|_1 = \sum_{\boldsymbol{\gamma}\in\beta_p} \left|y_{\boldsymbol{\gamma}}\right|$, which is moreover a good strategy to favour sparsity of the surrogate in high dimension, i.e. that it forces the minimization to favour low-rank solutions. In this paper, we rely on one of the several algorithms used to solve this constrained optimization problem, namely least angle regression (LAR)[61], which has been adapted to the context of PCE by Blatman and Sudret[62]. They have designed an adaptive hybrid form of LAR in order to obtain a sparse PCE representation that remains reasonably accurate even with for small experimental designs. Other more robust sparse representation approaches favor the early detection of data outliers[63]. In practice the adaptive PCE-LAR algorithm will be run at each time instant at which the data sample from the full thrombosis model is available. For each surrogate build, it will test through a polynomial order range and will select the optimal polynomial based on some validation criteria described hereafter. Thanks to the formulation, the retained polynomial basis will most likely be quite sparse (which means that a large portion of the modal coefficients will be null), resulting in a compact surrogate model. The leave-one-out (LOO) cross-validation error is a statistical learning technique, that is conveniently used for cases with small design of experiments (DoE). It consists in building N metamodels, each one created on a reduced experimental design $\boldsymbol{X}^l$, i.e. the training set obtained by removing a point $(\boldsymbol{X}^{(l)}, Y^{(l)})_{l\in\{1,2,\ldots,N\}}$, and comparing its prediction on the excluded scenario $\boldsymbol{X}^{(l)}$ with the real value obtained from the thrombosis simulation. These N errors are then averaged into a single value which may be collected for several time instants and different approximation bases for instance.

2.4.4 | Surrogate-based global sensitivity analysis

Once the modal coefficients are computed, moments, confidence intervals, sensitivity analysis and probability density function of the solution can be readily evaluated. Global variance-based sensitivity analysis may be performed to quantify the relative importance of each (or a group of) random input parameter to the uncertainty response of the system. The Sobol' functional decomposition of $Y = f(t, \boldsymbol{X})$ is unique and hierarchic. We have:

$$Y = f(t, \boldsymbol{X}) = \sum_{\boldsymbol{s}\subseteq\{1,2,\ldots N_d\}} f_{\boldsymbol{s}}(t, \boldsymbol{X}_{\boldsymbol{s}}), \tag{21}$$

where $\boldsymbol{s}$ is a set of integers such that $\boldsymbol{X}_{\boldsymbol{s}} = (X_{s_1}, \ldots, X_{s_N})$, with $N = \text{card}(\boldsymbol{s}) = |\boldsymbol{s}|$ and $f_{\varnothing} = f_0 = \mathbb{E}[Y]$. In this way, the variance of the response can be decomposed as[64]:

$$\mathbb{V}(Y) \equiv \sigma^2(t) = \sum_{\boldsymbol{s}\subseteq\{1,2,\ldots N_d\}} \sigma_{\boldsymbol{s}}^2(t), \quad \text{with} \quad \sigma_{\boldsymbol{s}}^2(t) = \mathbb{V}\left(\mathbb{E}\left[Y|\boldsymbol{X}_{\boldsymbol{s}}\right]\right) - \sum_{\substack{\boldsymbol{u}\subset\boldsymbol{s}\\ \boldsymbol{u}\neq\boldsymbol{s}\\ \boldsymbol{u}\neq\varnothing}} \sigma_{\boldsymbol{u}}^2(t), \tag{22}$$

where $\mathbb{V}$ and $\mathbb{E}$ are the variance and the expectation operators, respectively. The normalized Sobol' indices $S_{\boldsymbol{s}}$ are defined as[65]:

$$S_{\boldsymbol{s}} \equiv \frac{\sigma_{\boldsymbol{s}}^2(t)}{\sigma^2(t)} \quad \text{and} \sum_{\substack{\boldsymbol{s}\subseteq\{1,2,\ldots N_d\}\\ \boldsymbol{s}\neq\varnothing}} S_{\boldsymbol{s}}(t) = 1, \tag{23}$$

which measure the sensitivity of the variance of Y due to the interaction between the variables $\boldsymbol{X}_{\boldsymbol{s}}$, without taking into account the effect of the variables $\boldsymbol{X}_{\boldsymbol{u}}$ (for $\boldsymbol{u}\subset\boldsymbol{s}$ and $\boldsymbol{u}\neq\boldsymbol{s}$). In this work, we consider first- and total-order Sobol' indices. The first-order quantifies the effect of the single parameter alone X_s on the output. The total index of input variable X_s, denoted S_s^T, is the sum of all the Sobol' indices involving this variable: $S_s^T = \sum_{\boldsymbol{s}\subseteq\{1,2,\ldots N_d\}} S_{\boldsymbol{s}}$. This latter definition is not practical since it would result in computing each index separately. Instead, by denoting $S_{\tilde{s}}$ the sensitivity measure of all the variables *excluding* variable X_s, the total index can be rewritten as: $S_s^T = 1 - S_{\tilde{s}}$. Previous Sobol' indices can be evaluated by Monte-Carlo estimators, but require very large samples and introduce errors due to sampling. Instead, they can be obtained very straightforwardly directly from the polynomial chaos modal coefficients. Thanks to the orthonormality of the approximation basis, the Sobol' indices are explicitly obtained as combination of the PCE coefficients[66]. Despite this "exact" relation, the Sobol' indices are only accurate if the surrogate PCE is itself accurate.

3 | RESULTS

3.1 | Multi-constituent Thrombosis Simulations

The evolution in time of closure percentage and thrombus volume is shown in Fig.6 for 120 simulations. Closure percentage (Fig.6 A) is observed to follow a sigmoidal curve reaching a plateau of about 90% at time of 100-200 seconds. The variance among simulations appears to be greatest during the rapid growth portion of the curve, and virtually nil during the first and last 25 seconds (variance ≈ 0 and 1.4 times the corresponding mean respectively). It is noteworthy that the simulations do not reach full occlusion due to extremely high shear rates as the orifice cross section area approaches zero, and thrombus cleaning predominates.

In terms of the thrombus volume, Fig. 6B shows little growth during the first 100 seconds, the curves start to deviate significantly around 125 seconds reaching different levels of total thrombus volume between approximately 0.1 to 1.7 $m^3 \times 10^{-3}$.

Anticipating on the results of the following settings, both plots in Fig. 6 also show the surrogate mean, std-based confidence interval, and a box plot of the 25^{th} and 75^{th} percentiles. It can be observed that the surrogate model is able to correctly reproduce the trend observed in the multi-constituent thrombosis simulations (gray plots).

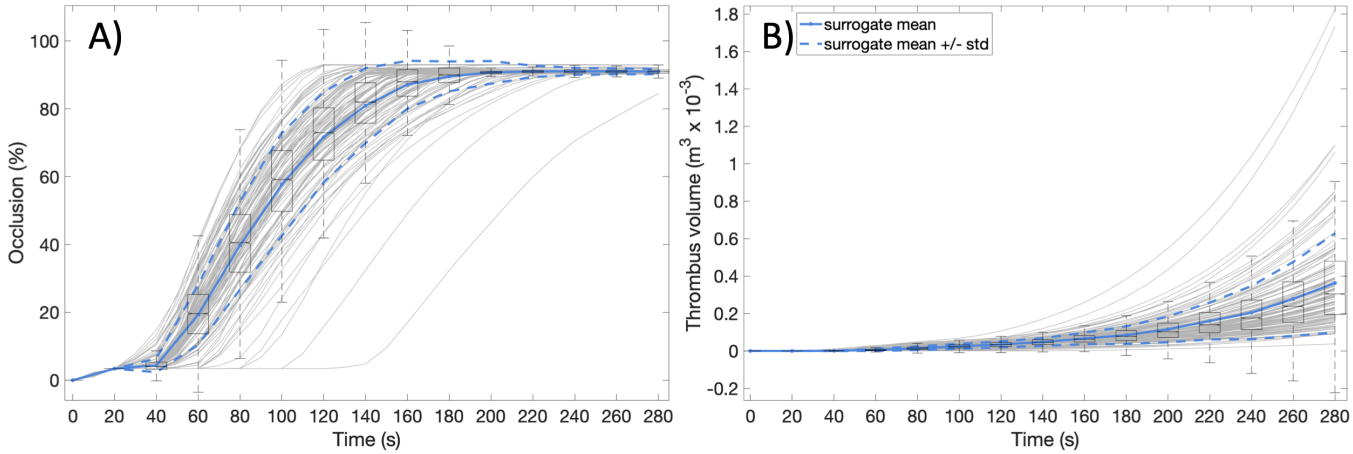

FIGURE 6 Output variables for 120 thrombosis simulations (gray lines), the blue solid and dashed lines are the mean and standard deviation of the surrogate model respectively, the box plots show the median and 25^{th} and 75^{th} percentiles of the surrogate model predictions, the whiskers in the box plots the variability between the upper quartile and upper maximum and the lower quartile and minimum of the surrogate model predictions. A) Occlusion percentage evolution in time B) Thrombus volume in the computational domain in time.

3.2 | PCE surrogate model training and thorough validation

In this paper, we aimed at obtaining a subtle balance between cost and predictive accuracy. We first carried out a preliminary study to determine a very moderate number of simulations to build our training database in order to construct a metamodel with small errors on various quantities. In addition, we were very drastic in our way of validating the metamodel by several means. We relied on LOO cross-validation error. We have also pursued a generalization test on a sample that was not used during training and that includes some extreme points (data points far away from the central tendencies of our training dataset). By doing so, we have quantified the confidence in these predictions. Finally, as we will see in a later section, we have compared our predictions with clinical data, cf. Section 3.4. We will describe in the following, the details of the various analyses.

To ensure that the parameter space $\boldsymbol{X}$ was uniformly explored, a Sobol' quasi Monte Carlo sequence was used to generate a DoE matrix. This choice is based on the fact that the classic Monte Carlo method does not depend on the number of dimensions, its convergence is slow and recent papers have shown that when applied to sensitivity analyses, Sobol' sequences exhibited faster convergence. While the observed benefit to convergence is moderate, Sobol' sequences are computationally less expensive to compute than Latin Hypercube Samples (LHS) and also have the benefit of being deterministic, which allows for better

reproducibility of results. In addition, a preliminary comparison was done using the aforementioned sampling techniques (See Supporting Information.) Then we computed the LOO error as a function of the training sample size using as QoIs the closure time and the thrombus volume as defined in Section 2.3. (See Figure 7.) This was repeated for five surrogate models of increasing complexity (increasing polynomial order p with truncation parameter, $q = 1$). Some readers may notice that some convergence curves with fixed polynomial order do not exhibit monotonous decrease despite increase in the training dataset size. This is due to the adaptive LARS approach, promoting sparsity by trimming the approximation basis. Small size basis (i.e. for low polynomial order) are sometimes affected by this optimization, resulting in small error fluctuations. Except for these very few models, the accuracy improved with increasing training size, reaching a point of diminishing returns at approximately 80-120 simulation.

In terms of model complexity, the best performance was found for polynomial order from $p = 2$ and 3. Further increasing the polynomial order was found to deteriorate accuracy, reflecting the limited sample size leading to overfitting. This motivated the use of an adaptive approach that searches, for each time step, an optimal combination within given ranges, i.e. polynomial orders $p \in \{1, 6\}$ and truncation parameters $q \in \{0.5 : 0.1 : 1\}$. This yielded lower error than fixed polynomial order and truncation parameter approximations. In any case, it should be reminded that with more data the surrogate model would increase in accuracy. Nevertheless, this pilot study demonstrated that 120 simulations were sufficient in order to reach reasonable accuracy when combined with an adaptive polynomial approach.

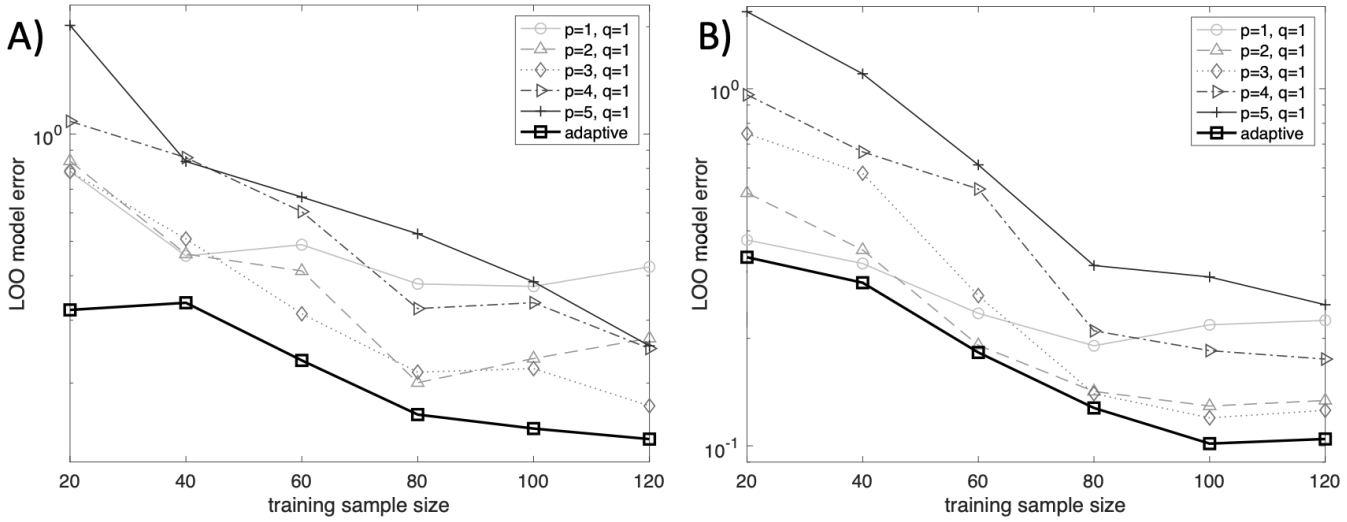

FIGURE 7 Time-averaged leave-one-out (LOO) cross-validation error of the parametric models as a function of the training sample size and model complexity. A) closure percentage error, and B) Thrombus Volume error. Adaptive metamodeling construction are more efficient than models with fixed complexity. They show reasonable accuracy for a budget of 120 full thrombosis simulations.

When considering the closure percentage and the thrombus volume QoIs, a series of PCE meta-models were constructed, one for each time step at which the QoI was saved during the simulations (for more information in time-dependent generalized polynomial chaos the reader is referred to the work of Gerritsma et al.[67]). For the closure percentage the non-zero PCE coefficients range from [1-25], on the other hand, for the thrombus volume QoI the range is [13-23]. To cross-validate the model for each time step, 125 points were sampled using the quasi-random Sobol' sequence, of which 120 points were used for the training set to build the surrogate model and 5 points used as the test set. For these 5 points, we have made sure that the testing data were sufficiently far away from the central tendency of the joint input distribution. The Mahalanobis distance was used to quantify how far the cross-validation points are from the original training dataset (See Table 3). All the points are at least 3 stds away from the mean of the training data-set, two of them are about 5 stds away. Five predictions using this methodology are shown in Figure 8, the dots correspond to the thrombosis simulation, the solid line is the PCE surrogate and the shaded area is the PCE confidence interval computed using the bootstrap technique [Marelli and Sudret[68]]. Producing a single prediction from each PCE surrogate is not very realistic due to the small training database and adaptive procedure used. Therefore, a confidence interval can be generated accordingly for each prediction. It is noteworthy that each surrogate model does not have the same

selected polynomial approximation space (e.g. not same optimal order p_{opt}), depending on the complex nature of the response to the parameters randomness along time.

Point	121	122	123	124	125
MD	5.32	3.97	4.87	3.3	3.86

TABLE 3 Mahalanobis Distance (MD) between the cross validation points and the training dataset mean in terms of standard deviations.

There are different approaches to combine polynomial chaos expansion and bootstrapping techniques. For the fast algorithm approach used for a large training sample, the sparse polynomial basis identified by the LARS algorithm during calibration is calculated only once from the available full experimental design, and bootstrapping is applied only to the final step, which consists in a classic ordinary least-square regression on the sparse basis. The full bootstrapping approach, recommended for smaller training sample, is more expensive but more accurate as it includes the estimation of the sparse PCE basis for *each* of the bootstrapped experimental designs. In this paper, the second approach is followed and prediction confidence intervals (±2std) are evaluated with 200 bootstrap replications. We notice that the simulations obtained with the full thrombus model do belong to these confidence intervals. The latter are wider for the thrombus volume variation.

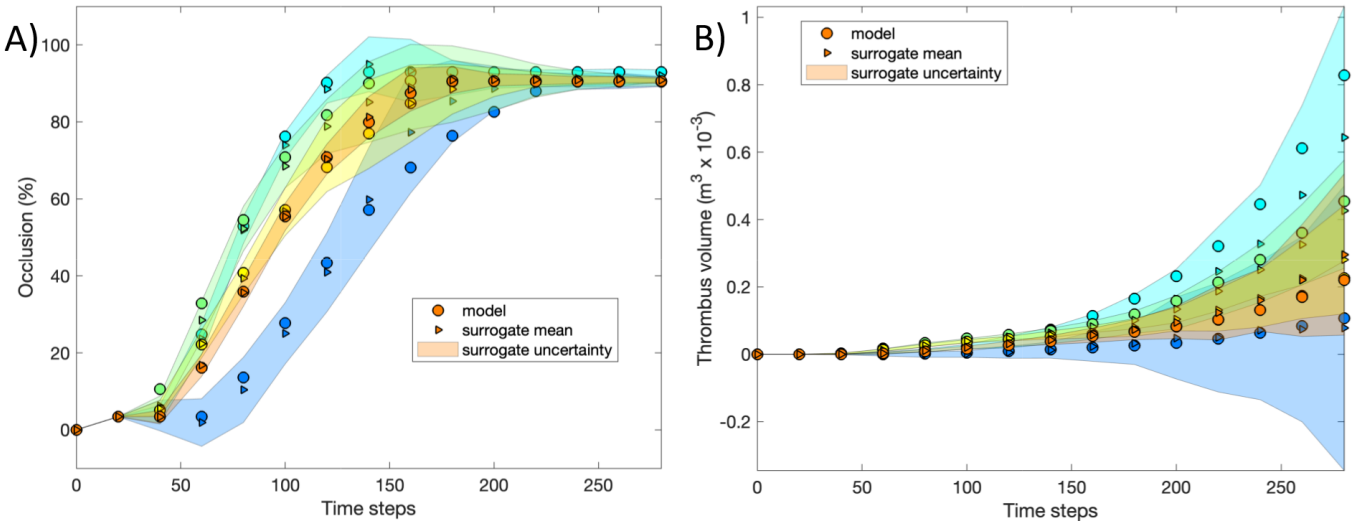

FIGURE 8 Cross validation on extreme events: generalization from PCE surrogate models (mean: triangles) compared to thrombosis simulations not included in the training dataset (circles). The shaded areas, obtained thanks to bootstrapping technique, represent the (2-std) confidence intervals associated with the meta-models. Most of the thrombosis simulations fall within the confidence intervals.

The accuracy of the PCE, evaluated by cross-validation with the LOO error criteria, remained for the occlusion percentage output under 20% for most cases with only one time step at 30% error (at $t = 200$ seconds). In the case of the thrombus volume output the LOO error remained under 10% reaching its maximum value by the last time step of the simulation. We consider that these errors showed that our surrogate was efficient considering that our initial space has $d = 15$ dimensions and we only used a moderate computational budget of $N = 120$ simulations.

In conclusion, these results provided sufficient validation for our PCE approach to continue with the sensitivity analysis and further applications.

3.3 | Sobol' Indices

The first order and total Sobol' indices for the 15 parameters computed using the closure percentage as QoI are shown in Fig. 9. In order to scale the effect of each parameter, the first Sobol' indices were multiplied by the variance computed through the PCE approximation. Considering the first order indices, seven parameters have a significant impact in the range $50s < t < 200s$ which is in line with the fact that most variations in the QoI are observed within this time range (see Fig. 6 A). The physical significance of the parameters identified by the first Sobol' indices is related to three main factors:

- **Thrombus constitution.** Resting platelet count (parameter 1) is the main constituent of the thrombus, therefore, it is understandably influential in the closure percentage.
- **vWF activity.** The parameters 3, 8, 11, 12, and 14 (vWF_c, $\dot{\gamma}_{vWF}$, t_{vWF}, Wi^{crit}_{eff}, and vWF^{crit}_s) control the unfolding dynamics of vWF and its subsequent impact in platelet deposition. The fact that these parameters were flagged signals the important role of vWF in high shear rate thrombosis.
- **Platelet-platelet adhesion.** The parameter 6 (k_{aa}) is the rate of platelet to platelet adhesion which directly influences the thrombus growth rate.

The Total Sobol' indices which evaluate the total effect of an input parameter, including all variance caused by its interactions with other parameters, are shown in Fig. 9 B. Significant effects for 11 out of 15 parameters are observed indicating non-negligible parameter interactions. Interestingly large effects are observed specifically after 180 seconds even-though the QoI shows little variation after this time. This could be explained by the high order approximations that were retained for these time steps.

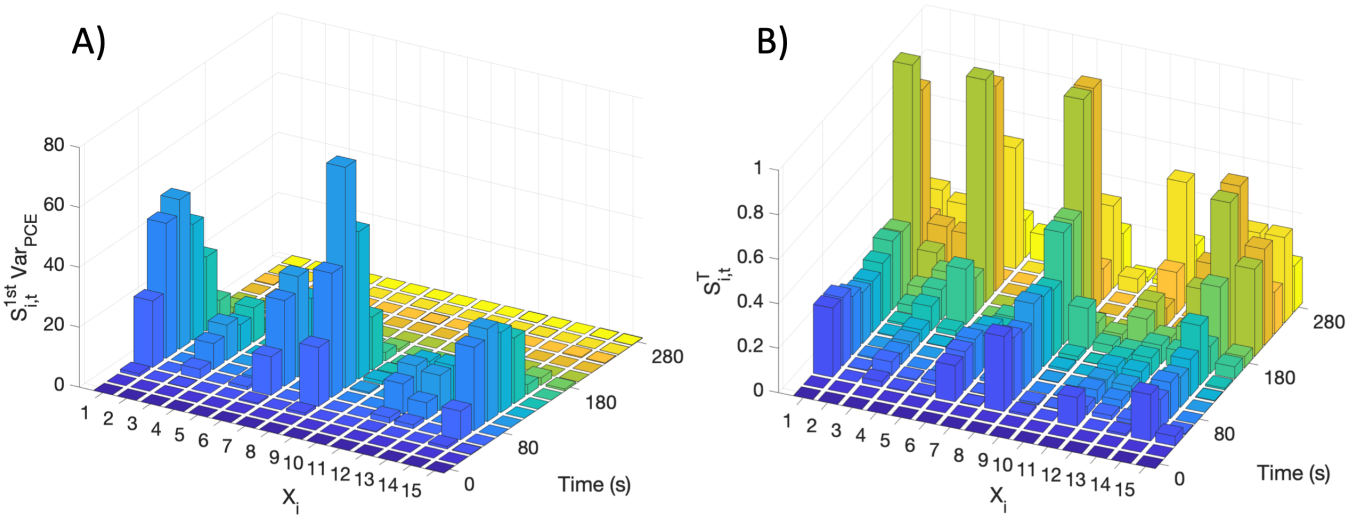

FIGURE 9 Sobol' indices evolution over time for the QoI closure percentage. A) First order indices multiplied by the output PCE variance. B) Total Sobol' indices.

Figure 10 shows the first order indices multiplied by the PCE variance and the Total Sobol' indices for the total thrombus volume QoI. In this case, only six parameters showed significant contribution to the output variations mainly at the last time steps which is in agreement with the behavior observed in the time evolution of the total volume QoI (see Fig. 6B). As in the previous QoI, the parameters that were identified are related to the thrombus constitution, the rate of platelet adhesion and vWF activity. These six parameters were also identified by the first Sobol' indices for the closure percentage QoI. Parameter 8 ($\dot{\gamma}_{vWF}$) that regulates vWF unfolding is not found to be influential in this case; although, a small contribution in the middle run of the thrombus formation is observed. This suggests that its role is only related to the initiation of the thrombus formation and not the subsequent growth of the thrombus. This is corroborated by the large value of its Total Sobol' index. (See Figure 10B.) The other six parameters found to be influential by the first Sobol' indices are also found to be influential considering their total

Sobol' indices. Parameters 9 and 7 ($\Delta\dot{\gamma}$ and k_{ra}) show a low but non-negligible impact, these parameters are related to direct vWF activity and platelet deposition respectively.

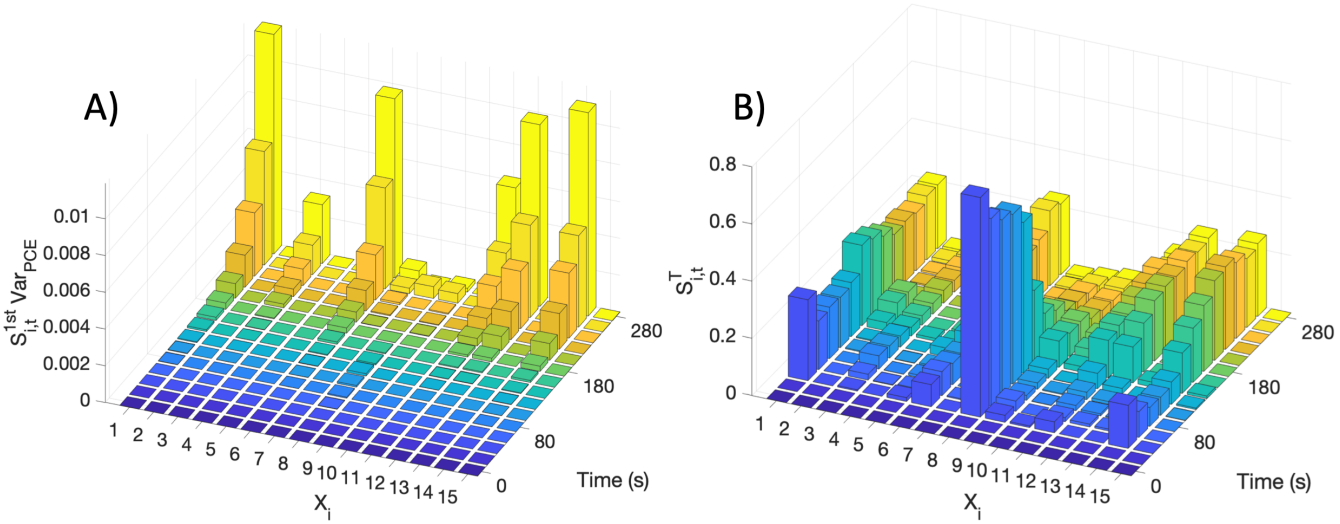

FIGURE 10 Sobol' indices evolution over time for the thrombus volume QoI. A) First order indices. B) shows the total Sobol' indices.

3.4 | Clinical Application: PFA-100® Closure Time

To investigate the practical relevance and the generalization of the current UQ framework, the surrogate model predictions for three clinical scenarios were compared to reference clinical data: normal blood, thrombocytopenia, and vWF disease. The PCE surrogate model was calibrated using the closure time of the PFA-100® as QoI as defined in Section 2.3. The full set of thrombosis simulations (125) were used to compute the PCE coefficients. Three sets of 100,000 points (parameters) as defined in Table 4 were drawn using the Monte Carlo sampling technique as implemented in the UQLab framework. The 13 supplementary model parameters that do not appear in Table 4 were held constant, as defined in Table 2.

Case	Parameter	Distribution (mean, standard deviation)
Normal	RP Resting platelet count	$\mathcal{N}(300\times10^3, 30\times10^3)$ Plt μL^{-1}
vWFD	vWF$_c$ (70 % of vWF concentration)	$\mathcal{N}(700, 70)$ nmol m^{-3}
Thrombocytopenia	RP (50% of Normal Resting platelet count)	$\mathcal{N}(150\times10^3, 15\times10^3)$ Plt μL^{-1}

TABLE 4 Definition of random parameters for the three cases.

Once the input databases were created for each case. The surrogate model was used to predict the 100,000 closure times for each set of parameters. The probability distribution of the PCE closure times for each scenario is presented in Figure 11 (solid red lines) superimposed with histograms derived from clinical data corresponding 172 patients, reported by Harrison et al.[42]. It should be noted that for the vWFD and Thrombocytopenia cases, the data were consolidated, as closure times equal to 300 were not taken into account since they are the maximum limit of the coagulation test indicating that the coagulation test failed. To facilitate the comparison a distribution was computed for the clinical data: a maximum likelihood estimate of a gaussian distribution was computed for the physiological case (large enough sample) and a kernel fit was obtained for the vWFD and thrombocytopenia cases (small sample). Even though the vWFD and Thrombocytopenia cases may not be statistically significant

($n = 26$ and $n = 6$ respectively) it can be observed that the surrogate model captures well the trend observed in the coagulation assay for the three cases; although for the thrombocytopenia case the PCE prediction lags the clinical data slightly.

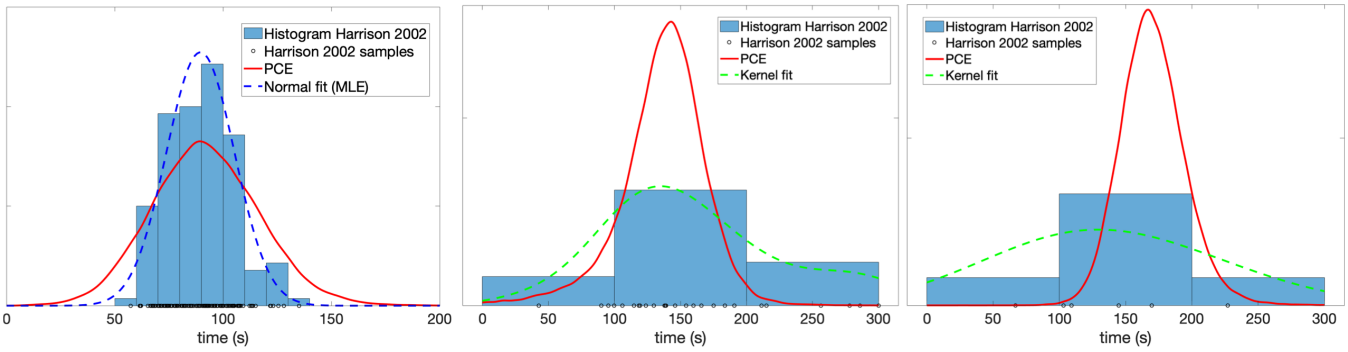

FIGURE 11 Distribution of closure times for simulated and clinically reported PFA-100® A) physiological case, B) vWF disease, and C) thrombocytopenia. Black circles along horizontal axes are the clinical data extracted from[42], a blue histogram was constructed using this data. The red line is the probability density function approximated from one hundred thousand realizations of the PCE surrogate model, the blue dashed line in A shows a Gaussian approximation (with a Maximum Likelihood Estimation MLE), and the green dashed lines in B and C are the kernel fits.

4 | DISCUSSION

Substantial progress has been made over the past decade in mathematical models of thrombosis which has enabled numerical simulation of a variety of clinically relevant thrombotic scenarios[69,70,71]. However, inherent uncertainties and assumptions of thrombosis models limit their translation to clinical practice and medical device development. This study investigated the impact of model parameter uncertainty in a thrombosis simulation by means of a polynomial chaos approximation. After extensive validation of the polynomial approximation, a global sensitivity analysis of 15 model parameters was performed. Six parameters showed significant influence in both quantities of interests considering their first Sobol' indices. This is in line with a recent study conducted by Melito et al.[29] in which the authors found that only 4 of the 9 parameters in the model of Menichini[7] were influential for predicting volume fraction of thrombus in a backwards step. However, investigation of parameter interaction via the total Sobol' indices revealed influence of a subset of the 9 "non influential" parameters according to the first Sobol' indices. This suggest that simplification of the model must consider both first and total Sobol' indices, lest it neglects the interdependence of parameters.

Several limitations are acknowledged in the current study. First, the thrombosis model itself involves several approximations[33], in which blood is treated as a Newtonian fluid, and the roles of red blood cells and fibrin formation are not explicitly considered. Yet, in reality, the closure time is likely to be influenced by RBC trapping within the clot, and possibly influenced by platelet margination induced by RBCs. Second, a fixed inlet velocity boundary condition to avoid numerical instabilities observed in the pressure driven case (more loyal to the PFA-100 system). The instabilities might be related to the PIMPLE algorithm, however, a more detailed study is needed. Since a robust setup was needed for the sensitivity analysis simulations, the fixed velocity inlet approach was used. In addition, the two methodologies yield very similar results (See Supplemental information). Third, a first triage of parameters was perform selecting only 15 parameters to perform the sensitivity study. Even though this selection was informed by our previous thrombosis studies[48,33,49,41] it remains somewhat arbitrary. Furthermore, the parameters excluded in this first triage step may have non-negligible parameter interactions with the 15 parameters selected. A possible way to better select this set of parameters is to perform a screening global sensitivity analysis with the Morris method as in Méndez Rojano et al.[27]. Fourth, the type of distribution and the magnitude of its variance that was assumed for the model parameters (10%) was somewhat arbitrary and was applied to all the parameters equally. In future studies, each parameter should be assigned its own characteristic standard deviation. In addition, the definition of closure time used in the simulations was based on 80% occlusion of the orifice, whereas in reality it would be 100%. This was necessary due to the simulations reaching an asymptotic value of

approximately 90% due to extremely high shear rates as the orifice diameter approaches zero. Finally, the clinical database for normal blood was constructed with n=172 patients; for the vWFD and thrombocytopenia, only n=26 patients and n=6 patients were available respectively. A larger sample size would improve the comparisons for vWFD and thrombocytopenia cases.

Despite its limitations, the PCE surrogate model demonstrated practical utility inasmuch as it permitted quantification of the uncertainty associated with a large number of parameters of a thrombosis model with economical computational cost. By contrast, it would have been very prohibitive to simulate all 300,000 sets of parameters with the full thrombosis model. Moreover, it was shown that the adaptive surrogate initially calibrated for certain parametric variabilities was nevertheless also capable of providing very reasonable predictions in parametric regions of lower probabilities. It is particularly noteworthy that despite the fact that the parametric distribution of the normal clinical case was centered outside the training confidence interval (estimated for this normal distribution as 1.3 times the RP mean training value $= 280 \times 10^3$ Plt μ L^{-1}), the surrogate model nevertheless predicts very well the clinical observations.

In conclusion this study showed that a PCE surrogate model trained with high fidelity thrombosis simulation can reproduce the trends observed in clinical data. These results encourage future studies using this methodology to investigate the influence of anti-platelet agents to identify scenarios that could achieve a balance between the risk of thrombosis and bleeding.

5 | ACKNOWLEDGMENTS

This research was supported by NIH R01 HL089456 and NIH R01 HL086918.

6 | DISCLOSURE

The authors declare no conflict of interest.

7 | DATA AVAILABILITY

The data that support the findings of this study are openly available in "Zenodo" at https://doi.org/10.5281/zenodo.5748289, including the clinical data from[42] which was digitized, and the uncertainty quantification code.

References

1. Nagareddy P, Smyth SS. Inflammation and thrombosis in cardiovascular disease. Current Opinion in Hematology; 2013.
2. Dal Sasso E, Bagno A, Scuri ST, Gerosa G, Iop L. The Biocompatibility Challenges in the Total Artificial Heart Evolution. *Annual Review of Biomedical Engineering* 2019; 21: 85–110.
3. Jaffer IH, Weitz JI. The blood compatibility challenge. Part 1: Blood-contacting medical devices: The scope of the problem. *Acta Biomaterialia* 2019; 94: 2–10.
4. Labarrere CA, Dabiri AE, Kassab GS. Thrombogenic and Inflammatory Reactions to Biomaterials in Medical Devices. *Frontiers in Bioengineering and Biotechnology* 2020; 8(March): 1–18.
5. Colman R. *Hemostasis and Thrombosis*. Lippincott Williams & Wilkins . 2006.
6. Leiderman K, Fogelson AL. Grow with the flow: A spatial-temporal model of platelet deposition and blood coagulation under flow. *Mathematical Medicine and Biology* 2011; 28(1): 47–84.
7. Menichini C, Cheng Z, Gibbs RG, Xu XY. Predicting false lumen thrombosis in patient-specific models of aortic dissection. *Journal of the Royal Society Interface* 2016; 13.
8. Yazdani A, Li H, Humphrey JD, Karniadakis GE. A General Shear-Dependent Model for Thrombus Formation. *PLoS Computational Biology* 2017; 13(1): e1005291.

9. Xu Z, Chen N, Kamocka MM, Rosen ED, Alber M. A multiscale model of thrombus development. *Journal of the Royal Society Interface* 2008; 5(24): 705–722.

10. Oleg V. K, Zhiliang X, Elliot D. R, Mark A. Fibrin Networks Regulate Protein Transport during Thrombus Development. *PLoS Computational Biology* 2013; 9(6).

11. Xu S, Xu Z, Kim OV, Litvinov RI, Weisel JW, Alber M. Model predictions of deformation, embolization and permeability of partially obstructive blood clots under variable shear flow. *Journal of the Royal Society Interface* 2017; 14(136).

12. Yazdani A, Li H, Bersi MR, et al. Data-driven Modeling of Hemodynamics and its Role on Thrombus Size and Shape in Aortic Dissections. *Scientific Reports* 2018.

13. Sorensen EN, Burgreen GW, Wagner WR, Antaki JF. Computational simulation of platelet deposition and activation: I. Model development and properties.. *Annals of biomedical engineering* 1999; 27(4): 436–448.

14. Storti F, Kempen vTHS, Vosse v. dFN. A continuum model for platelet plug formation and growth. *International Journal for Numerical Methods in Biomedical Engineering* 2014; 30: 634–658. doi: 10.1002/cnm

15. Danes NA, Leiderman K. A density-dependent FEM-FCT algorithm with application to modeling platelet aggregation. *International Journal for Numerical Methods in Biomedical Engineering* 2019; 35(9): 1–25.

16. Storti, F. and van de Vosse FN. A continuum model for platelet plug formation, growth and deformation. *International Journal for Numerical Methods in Biomedical Engineering* 2014; 30(September): 1541–1557.

17. Fogelson AL, Neeves KB. Fluid mechanics of blood clot formation. Annual Review of Fluid Mechanics; 2015.

18. Anand M, Rajagopal K, Rajagopal KR. A model for the formation and lysis of blood clots. *Pathophysiology of Haemostasis and Thrombosis* 2006; 34(2-3): 109–120.

19. Yesudasan S, Averett RD. Recent advances in computational modeling of fibrin clot formation: A review. *Computational Biology and Chemistry* 2019; 83: 107148.

20. Hansen KB, Shadden SC. Automated reduction of blood coagulation models. *International Journal for Numerical Methods in Biomedical Engineering* 2019; 35(10): 1–12.

21. Belyaev AV, Dunster JL, Gibbins JM, Panteleev MA, Volpert V. Modeling thrombosis in silico: Frontiers, challenges, unresolved problems and milestones. Physics of Life Reviews; 2018.

22. Sankaran S, Kim HJ, Choi G, Taylor CA. Uncertainty quantification in coronary blood flow simulations: Impact of geometry, boundary conditions and blood viscosity. *Journal of Biomechanics* 2016; 49(12): 2540–2547. doi: 10.1016/j.jbiomech.2016.01.002

23. Brault A, Dumas L, Lucor D. Uncertainty quantification of inflow boundary condition and proximal arterial stiffness–coupled effect on pulse wave propagation in a vascular network. *International Journal for Numerical Methods in Biomedical Engineering* 2017; 33(10): e2859. e2859 cnm.2859doi: https://doi.org/10.1002/cnm.2859

24. Nikishova A, Veen L, Zun P, Hoekstra AG. Uncertainty Quantification of a Multiscale Model for In-Stent Restenosis. *Cardiovascular Engineering and Technology* 2018; 9(4): 761–774. doi: 10.1007/s13239-018-00372-4

25. Steinman DA, Migliavacca F. Editorial: Special Issue on Verification, Validation, and Uncertainty Quantification of Cardiovascular Models: Towards Effective VVUQ for Translating Cardiovascular Modelling to Clinical Utility. *Cardiovascular Engineering and Technology* 2018; 9(4): 539–543. doi: 10.1007/s13239-018-00393-z

26. Danforth CM, Orfeo T, Mann KG, Brummel-Ziedins KE, Everse SJ. The impact of uncertainty in a blood coagulation model. *Mathematical Medicine and Biology* 2009.

27. Méndez Rojano R, Mendez S, Lucor D, et al. Kinetics of the coagulation cascade including the contact activation system: sensitivity analysis and model reduction. *Biomechanics and Modeling in Mechanobiology* 2019; 18(4): 1139–1153.

28. Link KG, Stobb MT, Sorrells MG, et al. A mathematical model of coagulation under flow identifies factor V as a modifier of thrombin generation in hemophilia A. *Journal of Thrombosis and Haemostasis* 2020; 18(2): 306–317.

29. Melito GM, Jafarinia A, Hochrainer T, Ellermann K. Sensitivity Analysis of a Phenomenological Thrombosis Model and Growth Rate Characterisation. *Avestia Publishing Journal of Biomedical Engineering and Biosciences (JBEB)* 2020; 7: 2020.

30. Campolongo F, Cariboni J, Saltelli A. An effective screening design for sensitivity analysis of large models. *Environmental Modelling and Software* 2007.

31. Saltelli A, Annoni P, Azzini I, Campolongo F, Ratto M, Tarantola S. Variance based sensitivity analysis of model output. Design and estimator for the total sensitivity index. *Computer Physics Communications* 2010; 181(2): 259–270.

32. Link KG, Stobb MT, Monroe DM, et al. Computationally Driven Discovery in Coagulation. *Arteriosclerosis, Thrombosis, and Vascular Biology* 2020(December): 1–8.

33. Wu WT, Jamiolkowski MA, Wagner WR, Aubry N, Massoudi M, Antaki JF. Multi-Constituent Simulation of Thrombus Deposition. *Scientific Reports* 2017.

34. Greenshields CJ. OpenFOAM. Tech. Rep. July, CFD Direct Ltd.; London, UK: 2021.

35. Babcock HP, Teixeira RE, Hur JS, Shaqfeh ES, Chu S. Visualization of molecular fluctuations near the critical point of the coil-stretch transition in polymer elongation. *Macromolecules* 2003; 36(12): 4544–4548.

36. Lippok S, Radtke M, Obser T, et al. Shear-Induced Unfolding and Enzymatic Cleavage of Full-Length VWF Multimers. *Biophysical Journal* 2016; 110(3): 545–554.

37. Fu H, Jiang Y, Yang D, Scheiflinger F, Wong WP, Springer TA. Flow-induced elongation of von Willebrand factor precedes tension-dependent activation. *Nature Communications* 2017; 8(1). doi: 10.1038/s41467-017-00230-2

38. Dong C, Kania S, Morabito M, et al. A mechano-reactive coarse-grained model of the blood-clotting agent von Willebrand factor. *Journal of Chemical Physics* 2019; 151(12). doi: 10.1063/1.5117154

39. Kania S, Oztekin A, Cheng X, Zhang XF, Webb E. Predicting pathological von Willebrand factor unraveling in elongational flow. *Biophysical Journal* 2021: 1–13. doi: 10.1016/j.bpj.2021.03.008

40. Sing CE, Alexander-Katz A. Dynamics of collapsed polymers under the simultaneous influence of elongational and shear flows. *Journal of Chemical Physics* 2011; 135(1). doi: 10.1063/1.3606392

41. Zhussupbekov M, Méndez Rojano R, Wu WT, Massoudi M, Antaki JF. A Continuum Model for the Unfolding of von Willebrand Factor. *Annals of Biomedical Engineering* 2021; 49(9): 2646–2658. doi: 10.1007/s10439-021-02845-5

42. Harrison P, Robinson M, Liesner R, et al. The PFA-100®: A potential rapid screening tool for the assessment of platelet dysfunction. *Clinical and Laboratory Haematology* 2002; 24(4): 225–232.

43. Mehrabadi M, Casa LD, Aidun CK, Ku DN. A Predictive Model of High Shear Thrombus Growth. *Annals of Biomedical Engineering* 2016; 44.

44. Steinlechner B, Dworschak M, Birkenberg B, et al. Platelet Dysfunction in Outpatients With Left Ventricular Assist Devices. *Annals of Thoracic Surgery* 2009; 87(1): 131–137.

45. Goodman PD, Barlow ET, Crapo PM, Mohammad SF, Solen KA. Computational model of device-induced thrombosis and thromboembolism. *Annals of Biomedical Engineering* 2005; 33(6): 780–797.

46. Zhang P, Sheriff J, Einav S, Slepian MJ, Deng Y, Bluestein D. A predictive multiscale model for simulating flow-induced platelet activation: Correlating in silico results with in vitro results. *Journal of Biomechanics* 2021; 117: 110275. doi: 10.1016/j.jbiomech.2021.110275

47. Manning KB, Nicoud F, Shea SM. Mathematical and computational modeling of device-induced thrombosis. *Current Opinion in Biomedical Engineering* 2021; 20: 100349. doi: 10.1016/j.cobme.2021.100349

48. Méndez Rojano R, Zhussupbekov M, Antaki JF. Multi-constituent simulation of thrombus formation at LVAD inlet cannula connection: Importance of Virchow's triad. *Artificial Organs* 2021; 45(9): 1014–1023. doi: 10.1111/aor.13949

49. Wu WT, Yang F, Wu J, Aubry N, Massoudi M, Antaki JF. High fidelity computational simulation of thrombus formation in Thoratec HeartMate II continuous flow ventricular assist device. *Scientific Reports* 2016. doi: 10.1038/srep38025

50. Manzoni A, Quarteroni A, Rozza G. Model reduction techniques for fast blood flow simulation in parametrized geometries. *International journal for numerical methods in biomedical engineering* 2012; 28(6-7): 604–625.

51. Adjoua O, Pitre-Champagnat S, Lucor D. Reduced-order modeling of hemodynamics across macroscopic through mesoscopic circulation scales. *International Journal for Numerical Methods in Biomedical Engineering* 2019; 35(12): e3274. e3274 cnm.3274doi: https://doi.org/10.1002/cnm.3274

52. Rasmussen CE, Williams CKI. *Gaussian Processes for Machine Learning*. The MIT Press . 2006.

53. Smola AJ, Schölkopf B. A tutorial on Support Vector Regression. NeuroCOLT; 1998.

54. Tatang M, Pan W, Prinn R, McRae G. An efficient method for parametric uncertainty analysis of numerical geophysical models. *Journal of Geophysical Research* 1997; 102: 21925-21932.

55. Ghanem RG, Spanos PD. *Stochastic finite elements: a spectral approach*. Courier Corporation . 2003.

56. Xiu D, Karniadakis GE. The Wiener-Askey polynomial chaos for stochastic differential equations. *SIAM journal on scientific computing* 2002; 24(2): 619–644.

57. Lucor D, Le Maître OP. Cardiovascular Modeling With Adapted Parametric Inference. *ESAIM: Proceedings and Surveys* 2018; 62. doi: 10.1051/proc/201862091

58. Shen J, Wang LL. Sparse Spectral Approximations of High-Dimensional Problems Based on Hyperbolic Cross. *SIAM Journal on Numerical Analysis* 2010; 48(3): 1087-1109.

59. Choi SK, Grandhi RV, Canfield RA, Pettit CL. Polynomial Chaos expansion with Latin Hypercube Sampling for estimating response variability. *AIAA journal* 2004; 42(6): 1191–1198.

60. Berveiller M, Sudret B, Lemaire M. Stochastic finite element: a non intrusive approach by regression. *European Journal of Computational Mechanics/Revue Européenne de Mécanique Numérique* 2006; 15(1-3): 81–92.

61. Efron B, Hastie T, Johnstone I, Tibshirani R. Least angle regression. *The Annals of statistics* 2004; 32(2): 407–499.

62. Blatman G, Sudret B. Adaptive sparse polynomial chaos expansion based on least angle regression. *Journal of Computational Physics* 2011; 230(6): 2345-2367.

63. Van Langenhove J, Lucor D, Belme A. Robust uncertainty quantification using preconditioned least-squares polynomial approximations with L_1-regularization. *International Journal for Uncertainty Quantification* 2016; 6(1).

64. Efron B, Stein C. The jackknife estimate of variance. *The Annals of Statistics* 1981; 9(3): 586-596.

65. Sobol IM. Sensitivity analysis for non-linear mathematical models. *Math. Modeling Comp. Experiment* 1993; 1: 407-414.

66. Marelli S, Sudret B. UQLab user manual – Polynomial chaos expansions. Chair of Risk, Safety and Uncertainty Quantification, ETH Zurich,Switzerland; 2021. Report# UQLab-V1.4-104.

67. Gerritsma M, Steen v. dJB, Vos P, Karniadakis G. Time-dependent generalized polynomial chaos. *Journal of Computational Physics* 2010; 229(22): 8333–8363. doi: 10.1016/j.jcp.2010.07.020

68. Marelli S, Sudret B. An active-learning algorithm that combines sparse polynomial chaos expansions and bootstrap for structural reliability analysis. *Structural Safety* 2018; 75: 67-74.

69. Peach TW, Ngoepe M, Spranger K, Zajarias-Fainsod D, Ventikos Y. Personalizing flow-diverter intervention for cerebral aneurysms: from computational hemodynamics to biochemical modeling. *International Journal for Numerical Methods in Biomedical Engineering* 2014; 30: 1387–1407.

70. Wan Ab Naim WN, Ganesan PB, Sun Z, et al. Flow pattern analysis in type B aortic dissection patients after stent-grafting repair: Comparison between complete and incomplete false lumen thrombosis. *International Journal for Numerical Methods in Biomedical Engineering* 2018; 34(5): 1–13.

71. Yazdani A, Deng Y, Li H, et al. Integrating blood cell mechanics, platelet adhesive dynamics and coagulation cascade for modelling thrombus formation in normal and diabetic blood. *Journal of The Royal Society Interface* 2021; 18(175): 20200834.